Atmospheric Compensation and Tracking Using Active Illumination

Charles Higgs, Herbert T. Barclay, Daniel V. Murphy, and Charles A. Primmerman

The U.S. Air Force is developing the airborne laser (ABL), whose mission is to engage and destroy theater ballistic missiles such as the SCUD while these missiles are in their boost phase. This mission capability requires high-energy laser propagation over long horizontal paths (200 to 300 km) through the upper atmosphere. To be effective in the presence of atmospheric turbulence, the ABL must utilize precision tracking and adaptive-optics compensation. Although the strength of atmospheric turbulence at ABL altitudes (35,000 to 45,000 feet) is relatively weak compared to sea level, the long horizontal laser-propagation paths create severe challenges for the adaptive-optics and tracking systems. An equally difficult challenge is created because the missile provides no beacon for the adaptive-optics and tracking systems. The target missile must be actively illuminated so that backscatter from the missile body can be used to form an image for the tracking system and provide a beacon for the adaptive-optics system. To understand this problem better and to improve system performance, we conducted propagation experiments at the Firepond telescope facility on Millstone Hill in Westford, Massachusetts. These tests utilized a 5.4-km horizontal propagation range between Millstone Hill and a fire tower in the town of Groton, Massachusetts. These experiments, which demonstrated for the first time active tracking and adaptive compensation under ABL conditions, suggest that the ABL can meet its mission goals and perform at levels required for effective theater missile defense.

The U.S. Air Force is developing the airborne laser (ABL) as a weapon system to engage and destroy multiple ballistic missiles at ranges as distant as several hundred kilometers. Current designs for the ABL envisage a Boeing 747 aircraft equipped with a 1.5-m nose-mounted beam director. The laser weapon will be a multimegawatt chemical oxygen-iodine laser operating at a wavelength of 1.3 microns. High-bandwidth adaptive-optics and tracking systems are required to correct for the beam jitter and higher-order phasefront aberration caused by turbulence in the atmosphere.

Because the missile being targeted provides no beacon (i.e., the missile is not cooperative) for the ABL adaptive-optics and tracking systems, the missile must be actively illuminated. This illumination is accomplished by using two separate illuminator laser systems. A track illuminator illuminates the nose-tip region of the missile, as shown in Figure 1. Backscatter from the track illuminator is collected and used as input to a high-bandwidth imaging tracker, and imaging-tracker output is used to correct the high-frequency tilt jitter induced by atmospheric turbulence.

An adaptive-optics illuminator illuminates a re-

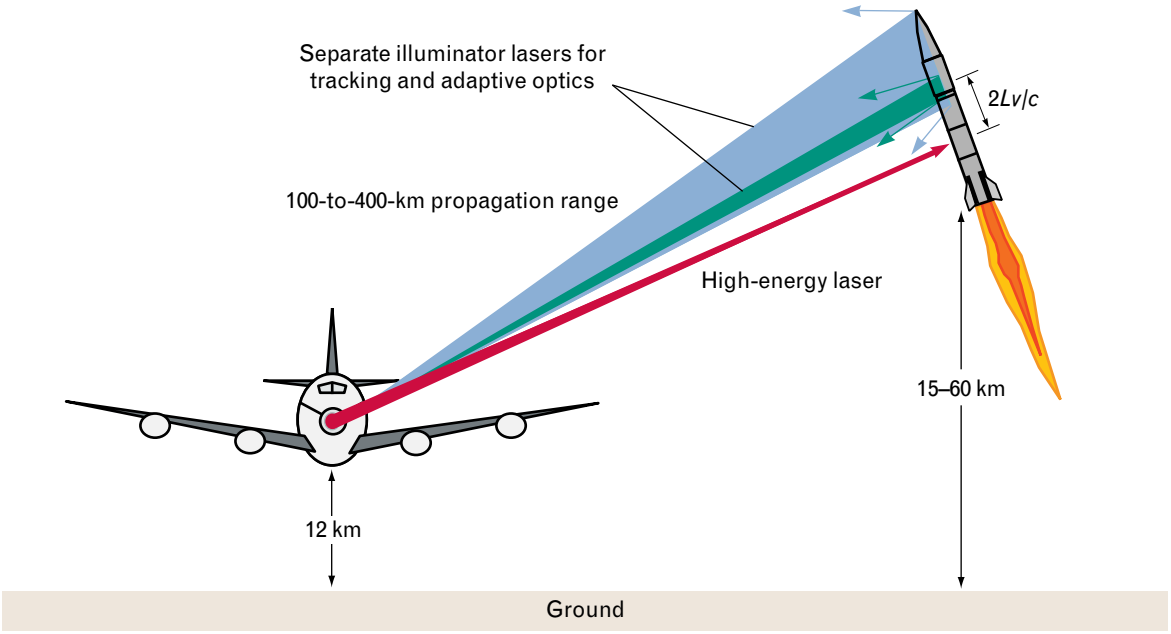

FIGURE 1. Airborne laser (ABL) illuminator geometry for active compensation and tracking of a boost-phase missile through atmospheric turbulence. The track illuminator (shown in blue) illuminates the nose-tip region of the missile to provide backscatter for the tracker. The adaptive-optics illuminator (shown in green) illuminates a region farther back on the missile body to provide a beacon for the adaptive-optics system. The high-energy laser (shown in red) is directed along the same path as the adaptive-optics illuminator return, but because of missile motion the laser strikes the missile at a point displaced by a distance $2Lv/c$, where v is the missile's velocity, L is its range, and c is the speed of light. The likely platform for the ABL will be a modified Boeing 747 aircraft, equipped with a 1.5-m nose-mounted beam transmitter and a multimegawatt laser operating at a 1.3-μm wavelength. The ABL can engage targets at altitudes between cloud top (approximately 15 km) and booster burnout (approximately 60 km).

gion farther back on the missile body to provide a beacon for the adaptive-optics system. Output from the adaptive-optics system is used to compensate the higher-order aberrations induced by atmospheric turbulence. The high-energy laser is directed along the same path as the adaptive-optics illuminator return; it strikes the missile at a point displaced by a distance $2Lv/c$, where v is the missile's velocity, L is its range, and c is the speed of light. This distance $2Lv/c$ is how far the missile moves during the time it takes for the illuminator return to reach the ABL and then for the high-energy laser beam to reach the missile.

In the familiar ground-to-space scenarios [1] in which adaptive optics works well, atmospheric turbulence is strong near the ground and weakens rapidly with increasing altitude. The ABL mission, however, requires missile tracking and laser propagation across long horizontal ranges over which atmospheric turbulence is weak but relatively constant. This type of laser-propagation path leads to severe intensity scintillation (i.e., temporal and spatial intensity fluctuations caused by turbulence-induced phasefront variations) of both the image of the boosting missile target that must be tracked and the high-energy laser that must engage it.

Making the ABL an effective weapon system requires technology advances in many areas. Some of the most challenging areas are aircraft payload design, high-energy laser technology, optical sensor development, and atmospheric compensation and tracking. This article concerns laser-propagation experiments and field studies we conducted at the Firepond telescope facility on Millstone Hill in Westford, Massachusetts. The purpose of these experiments was to better understand the problem of atmospheric compensation and tracking and to determine ways of improving ABL system performance.

Firepond experiments began in 1992 and were completed in 1997. The initial experiments were designed to investigate the limitations of basic atmo-

spheric compensation and tracking in the presence of severe scintillation [2]. These tests utilized a cooperative beacon that was produced by placing a laser-generated point source at the target. Results from these tests were important because they demonstrated that adaptive-optics compensation could be effective even for the challenging propagation scenarios expected for ABL. Beginning in 1995 the Firepond facility was reconfigured to include the more difficult problem of active illumination of the target, including illumination with multiple beams (see the sidebar entitled "Multibeam Illumination"). Initially, the experiments dealt only with active-tracking concerns [3]; the higher-order atmospheric compensation was performed by using point-source beacons. Results from these tests confirmed the benefits of multibeam illumination for active tracking. The most recent experiments included active illumination for both the tracking and the adaptive-optics systems [4]. The experimental configuration used for these tests conformed closely to the ABL contractor's concept for atmospheric compensation and tracking.

Parameter Scaling

Although the Firepond experiments were conducted on a ground-level laser-propagation path, the results are applicable to the ABL program because the experiment was scaled in such a way that the turbulence effects on the Firepond laser beam near the ground were the same as would be expected on the ABL beam at high altitude. One requirement for effective scaling is that the distribution of turbulence strength along the path should be the same at Firepond as it is for the ABL. For many ABL engagement scenarios, the target is engaged at altitudes much greater than the altitude of the ABL, in which case turbulence is weaker near the target than at the aircraft. For those cases, only approximate scaling can be achieved at Firepond, where the turbulence strength is expected to be fairly constant along the entire path. For some ABL scenarios, however, the target is engaged at low altitude, where the turbulence strength is expected to be nearly uniform along the entire path. These scenarios, which have the highest scintillation and tend to be the most stressing for the adaptive optics, can be well matched by the Firepond experiments. For nearly horizontal engagement scenarios, proper scaling of the Firepond experiments can be ensured by preserving four dimensionless parameters [5]: turbulence strength, normalized isoplanatic angle, Fresnel number, and scintillation strength (Rytov variance).

The turbulence strength, D/r_0, is the ratio of transmitter diameter to atmospheric coherence length. For the particular ABL scenario under study at Firepond the value of D/r_0 is expected to range between 2 and 6. The normalized isoplanatic angle, $\theta_0/[\lambda/D]$, is the ratio of isoplanatic angle to diffraction-limited angular resolution. Qualitatively, the isoplanatic angle can be thought of as the angular field of view over which high-fidelity imaging is possible. For the ABL scenario its value will range between 1.2 at weak levels of turbulence levels to 0.5 at higher levels of turbulence. It is unusual in adaptive-optics applications for this value to be less than unity, since such a low value means that even the system's diffraction-limited resolution is larger than the maximum angle over which good imaging can be achieved. The Fresnel number, $D^2/\lambda L$, is the square of the transmitter diameter divided by the product of wavelength and propagation range, and is an indicator of the importance of diffraction (the transformation of phasefront variations into intensity variations as the beam propagates). For the ABL scenario its value will range between 4 and 14. Finally, the scintillation strength, or Rytov variance, σ_R^2, is a measure of the severity of intensity scintillation caused by the distributed atmospheric turbulence. For the ABL scenario its value will range between 0.1 and 0.5.

Note that the atmospheric coherence length r_0, the isoplanatic angle θ_0, and the scintillation strength

Table 1. Propagation Parameters for the Firepond Facility and a Representative Airborne Laser Scenario

	Firepond	*ABL*
Transmitter diameter D	15 cm	1.5 m
Laser wavelength λ	0.5 μm	1.3 μm
Propagation range L	5.4 km	220 km

MULTIBEAM ILLUMINATION

ALTHOUGH THE STRENGTH of the atmospheric turbulence expected for airborne laser (ABL) engagement scenarios is relatively weak because of the expected high altitude of these encounters, the turbulence is uniformly distributed along the entire propagation path. One result of this distributed turbulence is strong intensity scintillation, which produces nonuniform illumination of the target. This nonuniform illumination has severe impact on the performance of an imaging tracker.

The multibeam illumination approach can reduce the intensity scintillation and improve tracker performance by propagating not one but many separate illuminator beams. As indicated in Figure A, the illuminator laser is divided into multiple beams, each of which is launched from a separate region of the transmitter. In practice, this division might be accomplished by using a single laser with specially designed optics and delay lines, or by using individual lasers. In the example shown here, four beams are produced from a single laser. In either case, each beam must be incoherent with respect to all the others. As the beams propagate toward the target, each beam samples a slightly different atmospheric path and, as a result, each produces a different target-plane irradiance profile. When these individual profiles are overlapped on target, they add incoherently to produce a more uniform irradiance profile.

The Firepond active-tracking tests reported here were performed by using a multibeam illuminator designed by Lockheed-Martin Missiles & Space, a member of the ABL contractor team. The design of the Lockheed illuminator permits the power from a

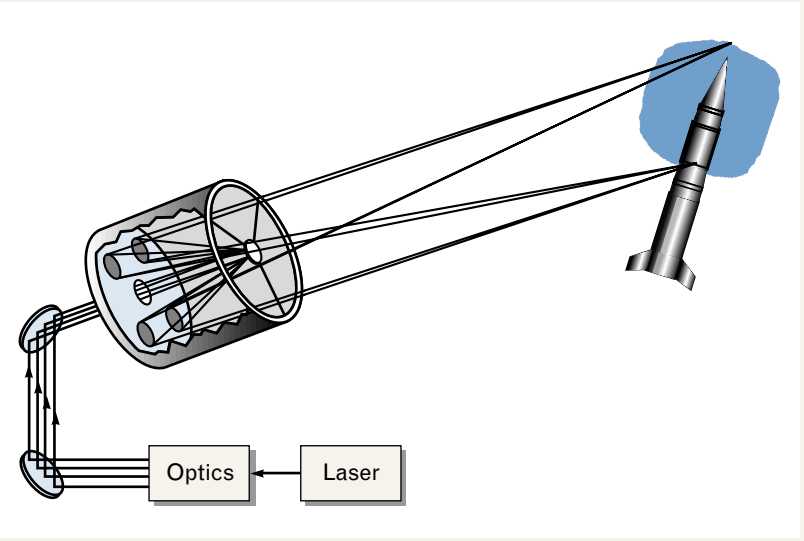

FIGURE A. Multibeam illuminator. In our approach to multibeam illumination, output from a laser is divided into multiple mutually incoherent beams. Each beam (four beams are shown in this example) is propagated from a separate region of the beam transmitter, but all beams are made to overlap on target.

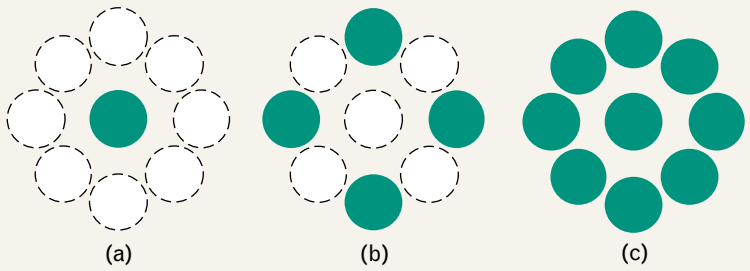

FIGURE B. Transmitter-beam configuration for multibeam-illuminator tests. These three diagrams show the multibeam footprint on the Firepond telescope primary mirror. Open-loop and closed-loop track data were recorded by using (a) one, (b) four, and (c) nine illuminators as shown. The total transmitted power was held constant for all tests.

single laser to be equally divided among nine beams, or be selectively diverted into one or more beams. Regardless of configuration, the total propagated power remains constant. For most of the multibeam-illuminator comparison tests performed at Firepond we used a single-beam, four-beam, or nine-beam configuration, as illustrated in Figure B.

Before active-tracking tests began, we characterized the target-plane irradiance of this illuminator by replacing the missile model with a flat screen and recording the illuminated screen with a gated CCD camera. Data were recorded with a single-beam, four-beam, or nine-beam illuminator configuration and for a range of turbulence strengths. These measurements involved recording many one-millisecond exposures at low frame rates in order to build up a collection of statistically independent realizations. Figure C shows examples of CCD camera data. In all three examples the total transmitted power was approximately the same. The turbulence strength was moderate with a Rytov variance of 0.25. The increase in target-plane irradiance uniformity for multibeam illumination is clearly apparent.

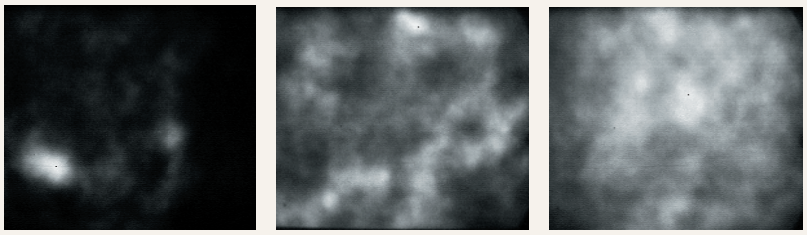

FIGURE C. Examples of multibeam-illumination target-plane irradiance profiles. Each image was recorded in the target plane by using either (a) one, (b) four, or (c) nine illuminator beams. Rytov variance was approximately 0.25 for each case, the total transmitted power was constant, and the exposure time was one millisecond. The uniform distribution of the irradiance profile in part *c* clearly would be more effective in illuminating a missile.

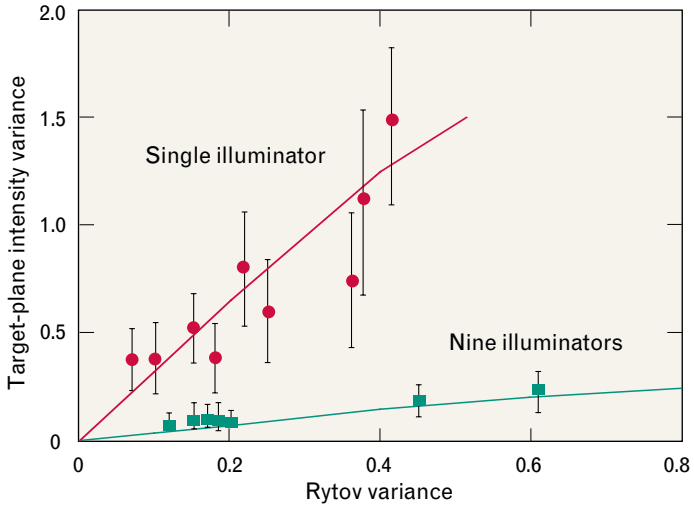

FIGURE D. Target-plane characterization measurements. Multibeam-illuminator data were obtained for single-beam illumination and nine-beam illumination. The data points are the average target-plane intensity variance, calculated from thirty one-millisecond realizations; the error bars represent the root-mean-square (rms) intensity variation for that particular thirty-frame data set. The solid lines are the predictions from steady-state propagation code.

For a more detailed comparison, the (normalized) intensity variance was calculated from each realization and averaged over a large number of samples. Figure D, which plots average intensity variance against Rytov variance, shows the results of this analysis. The data points are the average variances of thirty independent realizations; the solid lines are the predictions from propagation-code simulation. These results are in good agreement with propagation-code predictions and show a nearly threefold reduction in intensity variance when nine-beam illumination is used instead of single-beam illumination.

σ_R^2 are each related to the integrated strength of atmospheric turbulence along the propagation path, as follows:

$$r_0 = \left[0.423k^2 \int_0^L dz\, C_n^2(z) \left(\frac{z}{L}\right)^{5/3}\right]^{-3/5},$$

$$\theta_0 = \left[2.91k^2 \int_0^L dz\, C_n^2(z)(L-z)^{5/3}\right]^{-3/5},$$

and

$$\sigma_R^2 = 0.561k^{7/6} \int_0^L dz\, C_n^2(z)\, z^{5/6} (1 - \frac{z}{L})^{5/6},$$

where C_n^2 is the turbulence strength, L is the length of the propagation path, and k is the wave number $2\pi/\lambda$. The Fresnel number, on the other hand, depends only on propagation geometry. Therefore, the approach to parameter scaling taken at Firepond is to select the transmitter diameter D and laser wavelength λ to match the Fresnel number, and allow turbulence strength to vary so that the Rytov variance

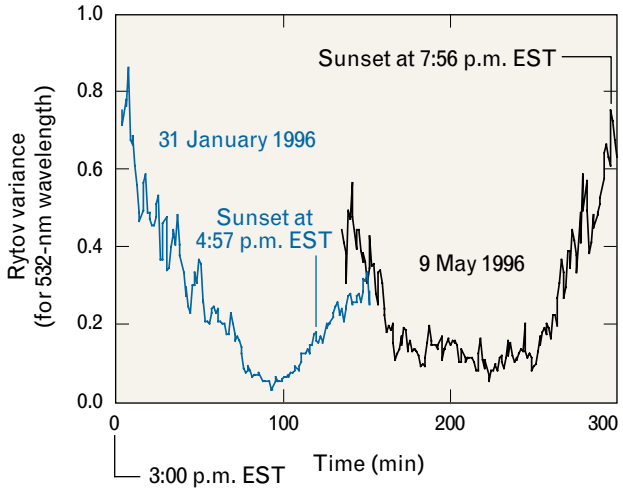

FIGURE 2. Typical levels of atmospheric turbulence at the Firepond telescope facility. This graph shows the variation in turbulence strength, as measured by a scintillometer and represented by the Rytov variance, during typical afternoon transitions on two selected days. During these transitions, solar heating of the earth's surface is nearly balanced by radiative cooling, and the strength of atmospheric turbulence is at a minimum.

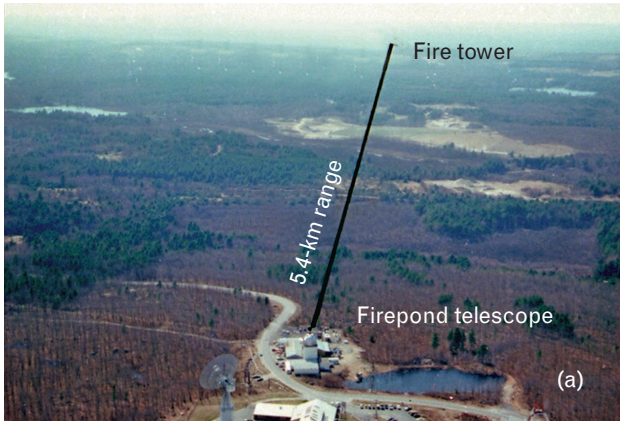

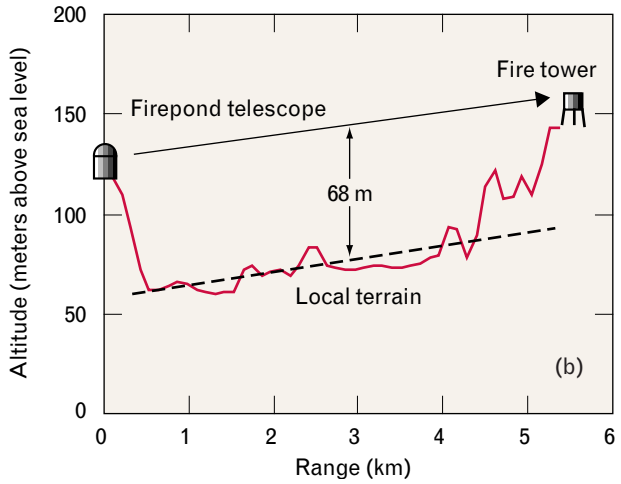

FIGURE 3. Firepond laser-propagation path. (a) Propagation experiments were conducted across the 5.4-km horizontal range between the Firepond telescope facility on Millstone Hill in Westford, Massachusetts, and a fire observation tower in Groton, Massachusetts. (b) The topographic profile of the propagation path indicates that the height of the laser beam averages approximately sixty-eight meters above the local terrain.

and the other parameters span the region of interest. Table 1 lists these choices of transmitter diameter, laser wavelength, and propagation range for the Firepond facility and a representative ABL scenario.

The time of day when the Rytov variance is in the appropriate range usually occurs during the hour or so before sunset. We refer to this period as the afternoon transition; it occurs when solar heating of the earth's surface is nearly balanced by its radiative cooling. During the transition period the strength of atmospheric turbulence passes through a minimum.

Figure 2 shows an example of atmospheric-turbu-

lence data for two selected days. The plot is a temporal history of the scintillation strength, presented here as Rytov variance. The raw data were recorded at ten-second intervals by a scintillometer lent to Lincoln Laboratory by the National Oceanic and Atmospheric Administration (NOAA) Wave Propagation Laboratory [6]. The NOAA scintillometer comprised a 0.95-μm diode laser and transmitter located at the Firepond facility, and a 20-cm-diameter receiver located in the fire tower. The scintillometer provides a measure of the average value of the atmospheric turbulence strength C_n^2 along the propagation path at 1-Hz rate. With an appropriate choice of wavelength and receiver diameter, the instrument can provide reliable estimates of turbulence strength up to a Rytov variance of nearly one. Beyond that value, saturation effects begin to reduce its accuracy. In addition to the scintillometer at the Firepond facility, we equipped each end of the propagation path with instruments to measure wind speed and direction, temperature, and relative humidity, which gave us additional important information about weather-related factors that influence turbulence and scintillation.

Figure 3 shows the topography along the laser-propagation path from the Firepond facility to the fire tower in Groton. The height of the laser beam above the local terrain is approximately sixty-eight meters over most of the path; terrain under the beam is mainly coniferous forest. On the basis of the uniformity of the terrain and the height of the beam above ground, we believe the turbulence is reasonably constant along the path.

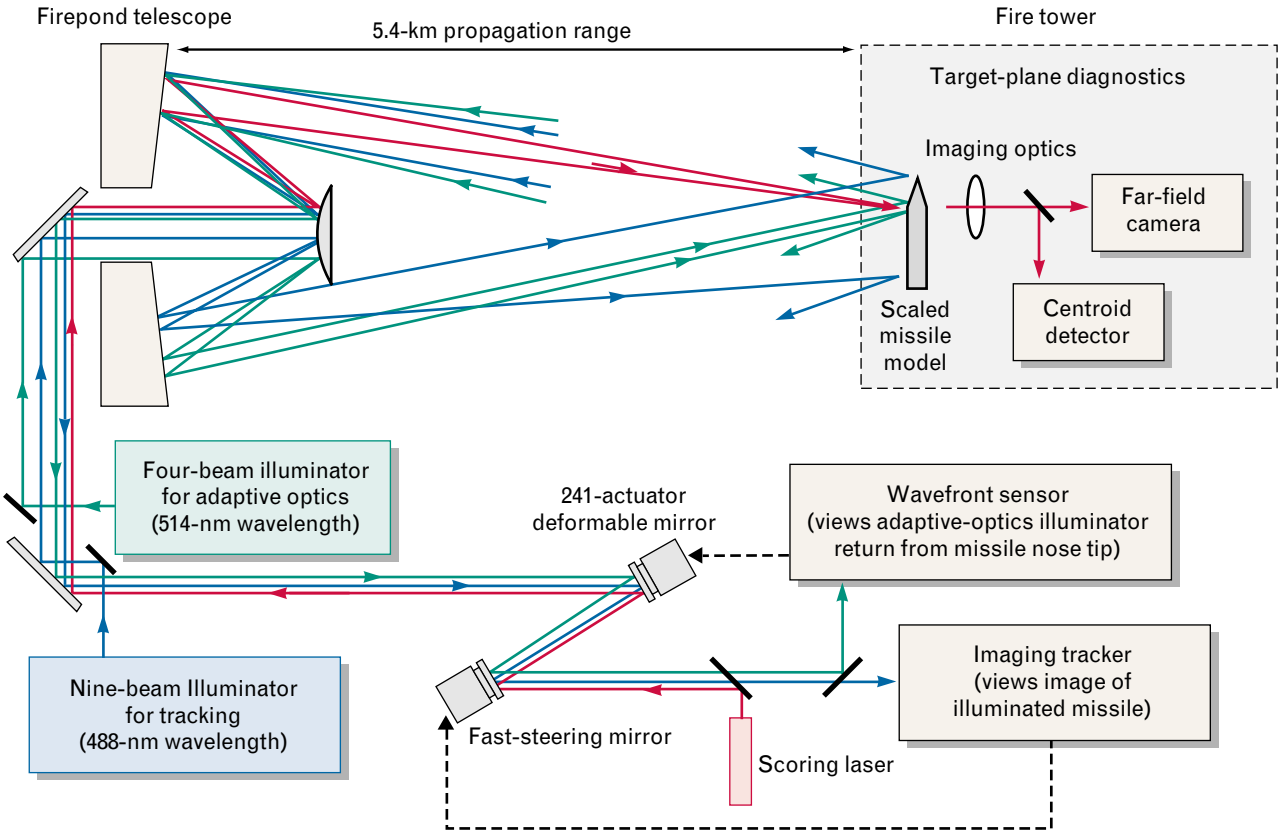

FIGURE 4. Firepond experimental configuration. Laser beams from the nine-beam track illuminator (blue) and the four-beam adaptive-optics illuminator (green) propagate from one quadrant of the Firepond telescope primary mirror across the 5.4-km test range to illuminate the scaled missile model in the fire tower. Backscatter from the missile is collected within a 15-cm aperture in another quadrant on the Firepond telescope primary mirror and directed to the imaging tracker and the wavefront sensor. The scoring-laser beam (red), which substitutes for the high-energy ABL in these experiments, samples the steering and deformable mirrors to receive its tilt and high-order correction, and is directed back toward the missile and the diagnostics in the fire tower.

Experimental Configuration

Figure 4 shows a diagram of the Firepond active-tracking and adaptive-optics compensation facility and horizontal propagation range. The 488-nm output from the multibeam track illuminator is merged into the Coudé path of the Firepond telescope and made to propagate from a 20-cm subaperture in the lower quadrant of the primary mirror. Similarly, the 514-nm output from the multibeam adaptive-optics illuminator is made to propagate from the right quadrant of the primary mirror. The track-illuminator and adaptive-optics-illuminator configurations are discussed in greater detail below.

Our target was a model missile, scaled so that the ratio of laser spot size to missile width approximated that expected for the ABL. The model missile comprised a 2.5-in cylindrical body with a 7-in-long conical nose. Its surface was coated with a reflection-enhancing material to reduce the power requirement on our illuminators. This scaled missile model was located in a fire tower at the end of the 5.4-km range. During active-tracking experiments, backscatter from the illuminated missile is collected within a 15-cm subaperture on the opposite side of the Firepond telescope primary mirror and relayed to the imaging tracker. Output from the imaging tracker is used to control a fast-steering mirror so that the scoring laser (the surrogate high-energy laser in these experiments) is precorrected for the turbulence-induced tilt jitter and directed back to the fire tower.

Performance Diagnostics

System performance is determined ultimately by the quality of the scoring-beam correction in the far field (i.e., at the missile). These determinations are provided by far-field irradiance diagnostics located in the fire tower, as shown in Figure 5(a). The diagnostics are in the small enclosure below the uppermost ranger station.

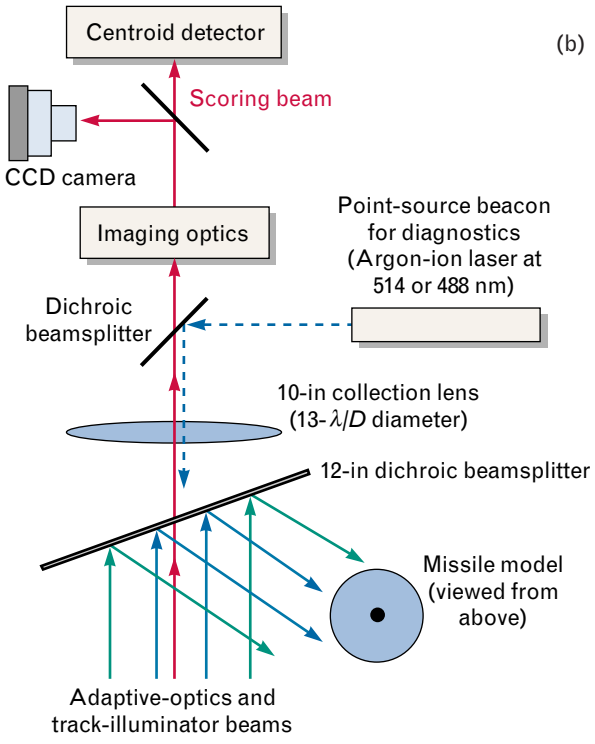

FIGURE 5. (a) Target fire tower and (b) far-field scoring-beam diagnostics and target geometry. The target diagnostics are located in the small enclosure below the fire-lookout station on top of the tower. The scoring beam passes through a dichroic beamsplitter and focuses onto the collection lens. The image of the spot is relayed into a CCD camera for far-field irradiance measurements, and into a centroid detector for pointing jitter measurements. The adaptive-optics and track-illuminator beams reflect from the beamsplitter and illuminate the scaled missile model.

Figure 5(b) illustrates the scoring-beam diagnostics and the target-plane geometry for illuminating the scaled missile model. Dichroic beamsplitters direct the scoring beam into the diagnostics and the illuminators toward the missile model. These beamsplitters also permit the transmission of a point-source beacon used for baseline performance measurements and for diagnostic comparisons. The image of the scoring-beam far-field irradiance is relayed into a 128 × 128-pixel CCD camera and a centroid detector. Both the CCD camera and the centroid detector have 13-λ/D fields of view, determined by the imaging optics and the collection lens. Data analyses have shown that this field of view is sufficient for closed-loop measurements of scoring-beam characteristics up to a Rytov variance of about 0.7. At higher levels of turbulence, spillover of the scoring beam outside the collection lens reduces the accuracy of the measurements.

Adaptive-Optics and Imaging-Tracker Configuration

Figure 6 shows a simplified schematic of the adaptive-optics and tracking control systems. Backscatter return from the adaptive-optics illuminator (green line) and from the track illuminator (blue line) was collected within the 15-cm scaled aperture and relayed to the deformable mirror and steering mirror. The 514-nm adaptive-optics illuminator return was directed into the wavefront sensor, and output from the wavefront sensor was reconstructed and used to drive the deformable mirror. The 488-nm track illuminator return was directed into the CCD camera for the imaging tracker and used to control the steering mirror. Output from an argon-ion laser provided a point-source beacon that could be utilized by either the adaptive-optics system or the imaging tracker, or recorded by the centroid detector as a diagnostic.

Lincoln Laboratory originally assembled the adaptive-optics system to support the Strategic Defense Initiative and used the system to conduct experiments at the U.S. Air Force Maui Optical Site on Mount Haleakala in Hawaii [7]. Table 2 provides some specific details of this system.

The imaging tracker used for these experiments is designated the Theater Missile Tracker (TMT). It was

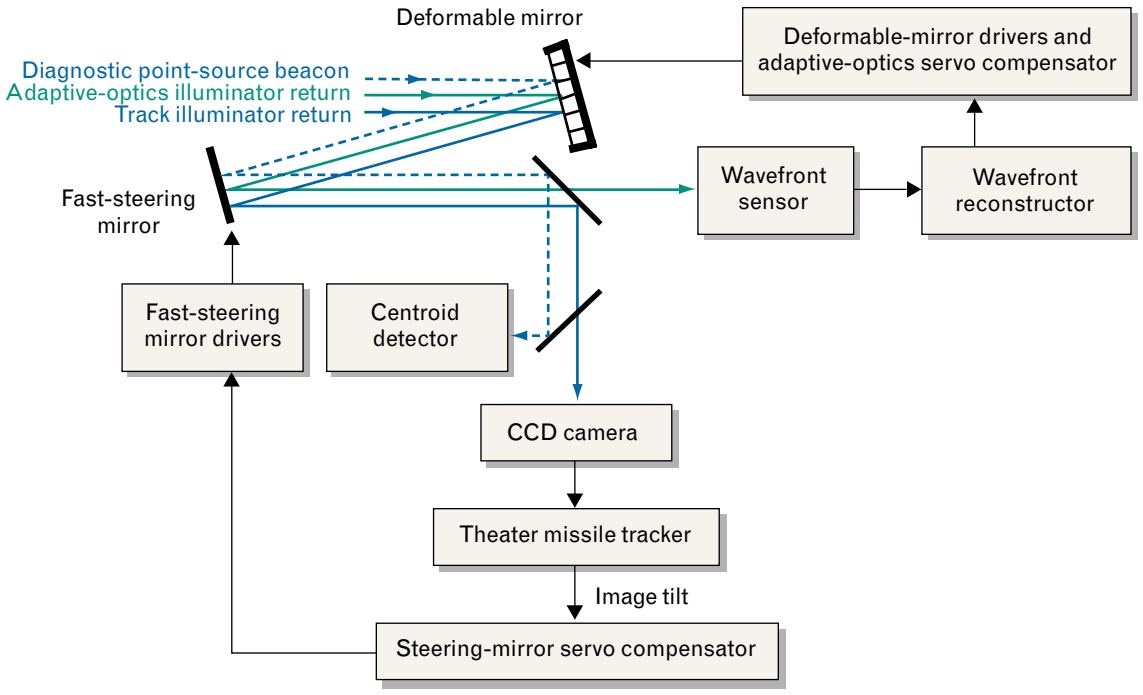

FIGURE 6. Diagram of the adaptive-optics and imaging-tracker systems. The adaptive-optics illuminator return (shown in green) is sensed by the wavefront sensor. Return from the track illuminator (shown in blue) is directed into the imaging tracker and into a diagnostic centroid detector. The track loops are controlled by output from the imaging tracker. Centroid-detector output is recorded as a diagnostic.

Table 2. Adaptive-Optics System Specifications

Deformable Mirror	
Design	ULE floating facesheet PMN actuators
Number of actuators	341 (241 active, 100 support)
Geometry	21 × 21 without corners
Stroke	4 microns
Wavefront Sensor	
Type	Hartmann Toe-to-tail configuration
Geometry	218 *x*-gradients 218 *y*-gradients
Detectors	Two 64 × 64 silicon CCDs 3-kHz sampling rate
Dynamic range	±2 waves per subaperture
Reconstructor and Servo	
Type	Matrix multiply
Servo design	Type 1 with digital accumulator
Bandwidth	120 Hz (0-dB crossover)

designed and built at the Air Force Phillips Laboratory and specifically configured to utilize output from a CCD camera built by Lincoln Laboratory. Essentially, the TMT is a high-speed data processor designed around a Mercury Quad i860s digital signal processor board. A Force Sparc 2c host workstation provides the user interface and is used for data post-processing and algorithm development.

The TMT can perform centroid calculations at frame rates of 1 kHz with missile-image data from the entire 64 × 64-pixel focal-plane array, or process a 16 × 16-pixel windowed subset of the data at a frame rate of 2 kHz. Other track algorithms have been implemented on the TMT, including the full, windowed, and binary centroid algorithms, and three variations of a correlation algorithm.

During closed-loop tracking, tilt error signals computed by the TMT are scaled appropriately and input to a Type-1 servo system. The servo-system output then provides the drive signals to control the pointing of a fast-steering mirror. Error-rejection measurements made with this tracking system show that its closed-loop bandwidth (0-dB crossover) is approximately 90 Hz. Table 3 provides some specific details of the TMT tracker.

Table 3. Tracker System Specifications

Design	Imaging
Detector	64 × 64-pixel silicon CCD
Pixel field of view	0.5 λ/D (1.7 microrad)
Algorithms supported	Centroid (full, windowed, binary) Leading edge, correlation
Processor	Mercury Quad i860s with Sparc 2c host
Servo	Type 1
Bandwidth	90 Hz (0-dB crossover)

Tracker and Adaptive-Optics Illuminator Configuration

Figure 7 illustrates the transmitter and target-plane beam profiles of the illuminator laser beams. The left side of the figure represents the Firepond telescope 48-in primary mirror, and shows how the multibeam illuminator for tracking propagates from the upper quadrant. The multibeam footprint is contained within a 20-cm-diameter circle and comprises nine individual 4-cm beams. Each beam, which is incoherent with respect to the others, is propagated to the target to form a 50-cm footprint on the missile model, as shown in the right side of the figure. The beams are aligned so that all the far-field patterns overlap on target.

Similarly, the multibeam illuminator for adaptive optics is propagated from the right quadrant of the primary mirror. Its footprint comprises four individual 4-cm beams contained within a 15-cm-diameter circle. As with the track illuminator, each adaptive-optics illuminator beam is incoherent with respect to the other beams. As indicated in the right

figure, each beam is directed toward the missile model and aligned so that all the far-field patterns overlap to form a 10-cm spot.

The reflected return from both illuminators is collected within a 15-cm scaled aperture located in the lower quadrant of the primary mirror. The outgoing scoring beam is propagated from this same aperture and directed back along the path of the adaptive-optics illuminator return.

Having the multibeam illuminators in one section of the Firepond telescope and the scoring beam in a separate section is not just an experimental convenience. It also results in the track illuminator experiencing a different atmospheric-turbulence profile from that seen by the scoring beam. This feature is important in order for the Firepond experiments to simulate ABL scenarios properly. For the ABL, the illuminators are likely to share the same transmitting aperture as the high-energy laser. The motion of the aircraft and target during the round-trip time of flight, however, will mean that the outgoing illuminators will not follow the same path as the high-energy laser and will not, therefore, be corrected for atmospheric turbulence.

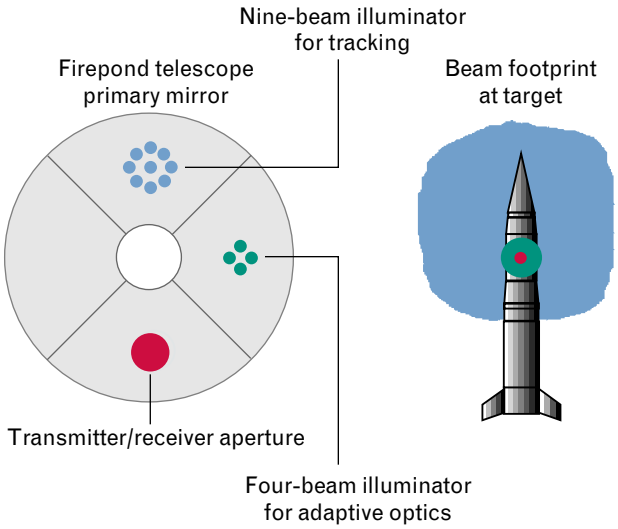

FIGURE 7. Transmitter and target-plane laser beam geometry. The drawing on the left indicates the positions of the nine-beam track illuminator, the four-beam adaptive-optics illuminator, and the scoring beam on the primary mirror of the Firepond 48-in telescope. The drawing on the right indicates the target-plane footprints of these beams as they fall on the scaled missile model in the fire tower.

Test Overview

We performed our initial tests with point-source beacons for both adaptive-optics and tracking, as discussed earlier in the article. Results from these tests demonstrated for the first time the feasibility of adaptive-optics compensation under atmospheric-turbulence conditions expected for the ABL. Point-source-beacon results also provided baseline performance measurements against which the active-tracking and active-compensation results could be compared.

The first active-illumination tests addressed tracking issues. A nine-beam illuminator (provided by Lockheed-Martin) was installed along with the TMT imaging tracker. The adaptive-optics system continued to utilize the point-source beacon. In the beginning we performed tests with a number of different track-illuminator configurations. Initially, the missile model was illuminated with a single illuminator; subsequent tests were performed with four-beam and nine-beam illumination. Results from these measurements have quantified the benefits of multibeam illumination for tracking [3].

Following the illuminator-configuration tests, we performed active-tracking tests to compare a variety of different tracking algorithms. All these tests were configured for nine-beam illumination. Data were recorded while using the conventional centroid algorithm, as well as variations such as the binary centroid algorithm. Various correlation algorithms were compared along with a number of algorithms supplied by the ABL contractor. Results of these tests are not reported here.

Next we installed a second multibeam illuminator for the adaptive-optics system. To simplify experimental procedures, we performed initial active-compensation tests with active illumination while the tracking was done with the point-source beacon. These tests addressed the impact of the extended target on adaptive-optics performance [4]. Data were recorded over a wide range of Rytov variances and with two adaptive-optics illuminator configurations: single-beam and four-beam illumination.

Finally, we performed tests with a configuration closely resembling that planned for the actual ABL system: one multibeam illuminator for tracking and a

second multibeam illuminator for adaptive-optics compensation. Results from these tests demonstrate that conventional adaptive-optics and tracking, performed with active illumination of the target missile, effectively compensate turbulence-induced phase and tilt fluctuations under ABL conditions.

Active-Tracking Experimental Results

The discussion of our active-tracking results begins with an overview of tests designed to compare different illuminator configurations. Both open-loop and closed-loop tests were performed with either single-beam, four-beam, or nine-beam illumination; these tests were designed to quantify the performance benefits of multibeam illumination. The tracker utilized the conventional centroid algorithm for all illuminator comparison tests.

Open-Loop Imagery

Before the TMT tracker was integrated into the Firepond tracking system, we made preliminary measurements to help quantify the effects of multibeam illumination and to prepare for closed-loop active-tracking tests. For these measurements, all performed open loop (i.e., with the tracking servos off), we illuminated the missile model with either one or nine illuminator beams, and collected images under a variety of atmospheric-turbulence strengths. Data were recorded over a range of Rytov variances between approximately 0.07 and 0.6. Each data record contained about 120 CCD images at a resolution of 64 × 64 pixels and an integration time of one millisecond.

Figure 8 shows one example of these image data, in this case for Rytov variance of approximately 0.2. The image in Figure 8(a) was recorded with only a single beam illuminating the missile model; the image in Figure 8(b) was recorded with nine illuminating beams. Both images are taken from single frames of the CCD camera. The image in Figure 8(b) illustrates the ability of a multibeam illuminator to reduce image scintillation; the image is a better resemblance of the missile nose tip, but is still distorted. Images like these clearly demonstrate that, even with the improvement provided by multibeam illumination, precision tracking under ABL conditions is a difficult challenge.

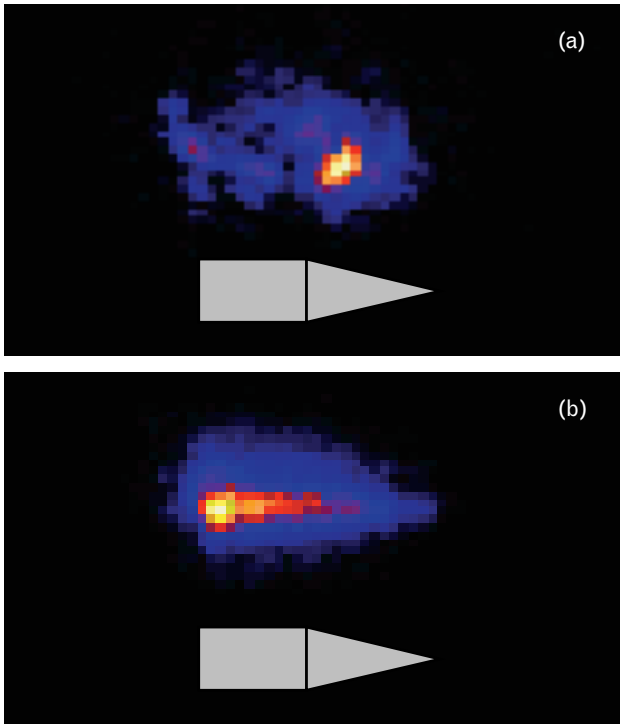

FIGURE 8. Missile model images produced with (a) single-beam illumination and (b) nine-beam illumination. The drawing in each figure shows the shape and orientation of the nose tip. In both cases the total illuminator power was the same. Multibeam illumination of the missile model reduces image scintillation, but the image is still distorted.

Open-Loop Spectra

The reduction in scintillation and its benefit to an imaging tracker can be quantified by comparing tilt-jitter spectra derived simultaneously from missile-image data (like those shown in Figure 8) and point-source-beacon data. Figure 9 shows such a comparison. In this case, a single beam was used to illuminate the scaled missile model during moderate turbulence (the Rytov variance was approximately 0.2). With the track loops open, we recorded thirteen-second time histories of data from the imaging tracker (viewing the illuminated missile model) and simultaneous data from the centroid detector (viewing the point source).

Figure 9(a) compares a tilt spectrum for the missile's transverse axis with a spectrum derived from the simultaneously recorded point-source data. Figure 9(b) shows a similar comparison for the missile's longitudinal axis. Tilt errors derived from the missile's

transverse axis clearly resemble those of the point source, and have similar cumulative power: 0.94 and 0.76 λ/D rms, respectively. Given the narrow angular extent of the missile's transverse axis, this result is not surprising.

This similarity of the missile's transverse-axis tilt spectrum to that of a point source does not, however, extend to the missile's longitudinal axis. Comparison of the two tilt spectra reveals a significant increase in cumulative power for tilt signals derived from the illuminated missile image: 1.5 λ/D rms from the missile image versus 0.98 λ/D for the point source. This increase in tilt jitter, which starts at frequencies near 10 Hz and extends out to the noise floor of the instruments, is the direct result of the scintillation seen in the images recorded with single-beam illumination shown in Figure 8(a).

Figure 10 shows a similar comparison when nine beams are used to illuminate the scaled missile model. All these data were recorded open loop under moderate turbulence conditions (the Rytov variance was approximately 0.23).

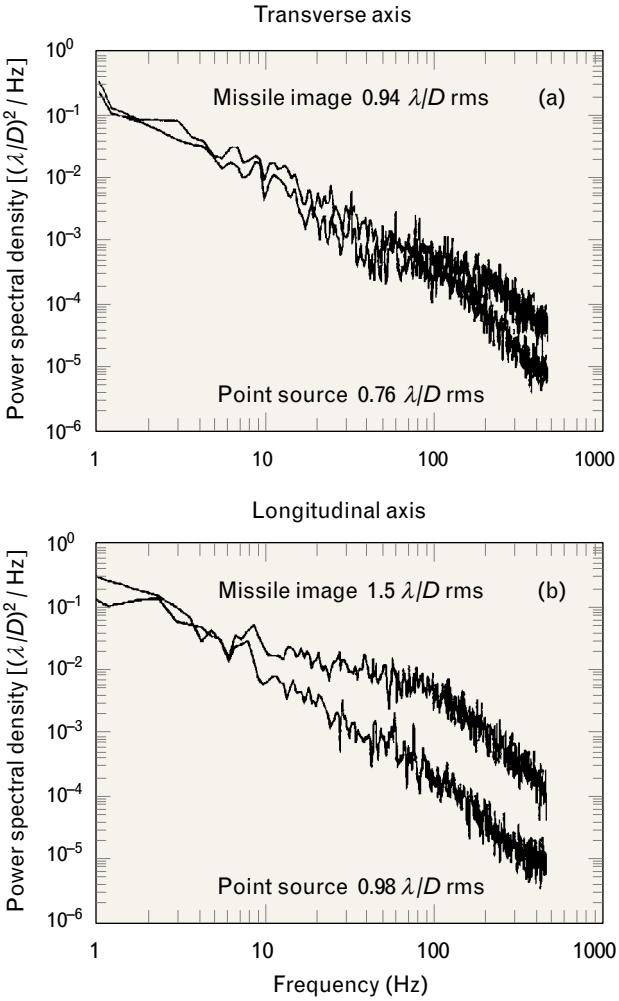

FIGURE 9. Comparison of point-source jitter spectra and missile-image jitter spectra using single-beam illumination of the missile model. Results are shown for (a) the missile's transverse axis and (b) the longitudinal axis. The tilt spectra were calculated from simultaneously recorded output from the imaging tracker and the centroid detector. The imaging tracker viewed only the illuminated missile; the centroid detector viewed the point-source beacon.

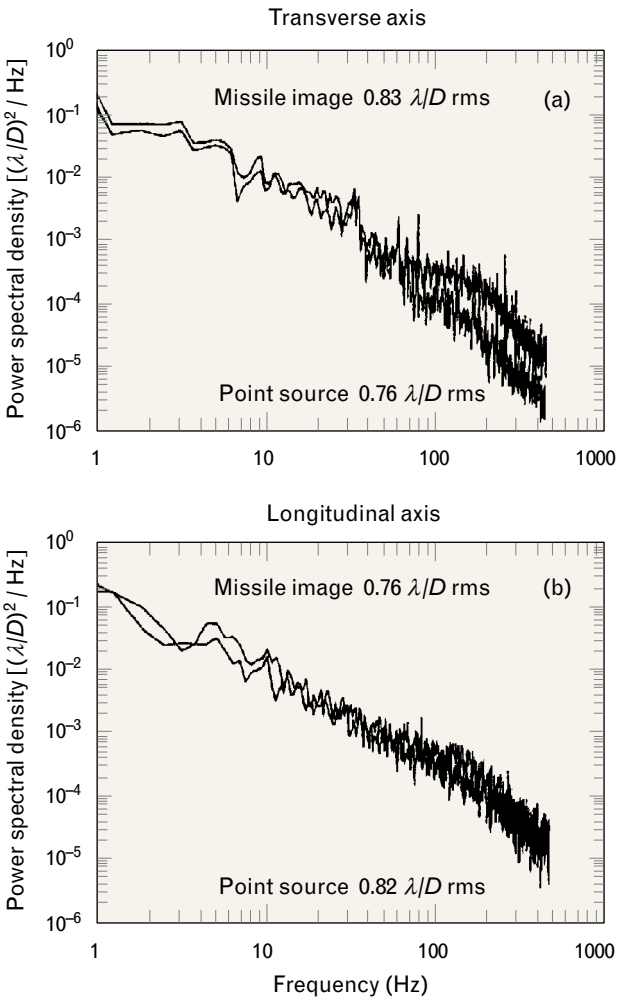

FIGURE 10. Comparison of point-source jitter spectra and missile-image jitter spectra using nine-beam illumination of the missile model. Results are shown for (a) the missile's transverse axis and (b) the longitudinal axis. The missile-image jitter spectra and the point-source jitter spectra were simultaneously recorded, similar to the way the jitter spectra data for single-beam illumination tests were recorded in Figure 9.

As with the single-beam illumination spectra data shown in Figure 9, tilt power spectra derived from the transverse axis of the missile are similar to those computed from point-source tilt data. Both contain about the same cumulative power: approximately 0.83 and 0.76 λ/D rms, respectively. With nine-beam illumination, however, this similarity in tilt spectra now extends to the longitudinal axis as well. The overall cumulative powers are similar: 0.76 λ/D rms for the missile versus 0.82 λ/D for the point source. The important point is that illumination with nine beams has significantly reduced the scintillation that might otherwise appear as tilt to the imaging tracker.

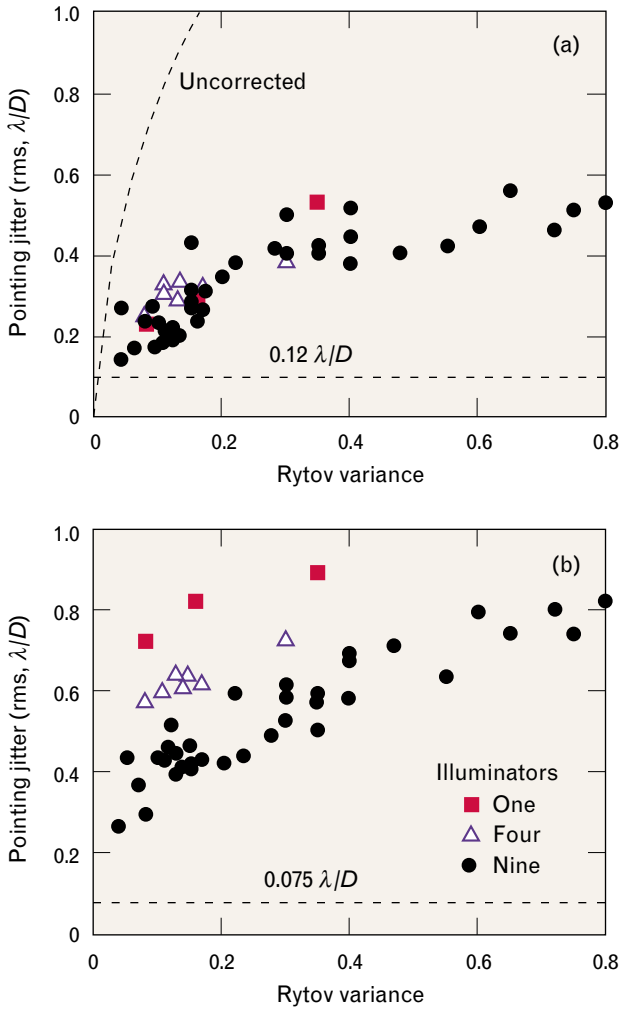

FIGURE 11. Active-tracking results for multibeam illumination. The plots show residual pointing jitter obtained with single-beam, four-beam, or nine-beam illumination. Results are shown for (a) the missile's transverse axis and (b) the missile's longitudinal axis. In all cases tracking was performed by using a centroid algorithm. The horizontal line in each plot indicates the measured baseline performance limit along that axis for point-source tracking in the absence of atmospheric turbulence.

Closed-Loop Comparisons

The results discussed in this section were obtained with the image tracker loops closed, using the centroid algorithm. Figure 11 summarizes these results, with residual scoring-beam pointing jitter plotted against Rytov variance derived from NOAA scintillometer data. Figure 11(a) shows the pointing jitter corresponding to the missile's transverse axis; Figure 11(b) shows the residual pointing jitter along the missile's longitudinal axis. The different plotting symbols in the legend specify the illuminator configuration. The horizontal dotted line in each plot indicates our system's measured baseline performance limit along that axis for point-source tracking in the absence of atmospheric turbulence. For the axis corresponding to the missile's transverse dimension, this limit is 0.12 λ/D; for the missile's longitudinal axis, this limit is approximately 0.075 λ/D. The appendix entitled "Baseline Performance Measurements" discusses the origin of these performance limits and how they were determined.

Note that the residual pointing jitter corresponding to the missile's transverse axis, shown in Figure 11(a), appears insensitive to illuminator configuration. No clear trends are evident that would indicate an improvement from multibeam illumination. We believe that this insensitivity to illuminator configuration comes from the fact that the missile transverse dimension effectively confines the illuminator spot to a size comparable to $L\lambda/D$, and thus the active beacon looks like a point source in the transverse direction. Indeed, tracking results obtained by using an actual point-source beacon closely follow the active-tracking results for the missile's transverse axis.

For the missile's longitudinal axis, however, the data show a clear dependence on illuminator configuration. Results obtained with nine-beam illumination are consistently better than those obtained with four-beam illumination. In turn, the four-beam results are consistently better than those obtained with single-beam illumination.

Active-Compensation Experimental Results

As we discussed earlier, active-compensation tests utilized a second illuminator to provide the beacon for the adaptive-optics system, as shown in Figure 4. For these tests the adaptive-optics illuminator at 514-nm wavelength (in this case providing four beams) was inserted into the Coudé path at the base of the telescope tower and made to propagate from the right quadrant of the telescope primary.

The design of the four-beam illuminator for adaptive optics is similar to the nine-beam track illuminator—each of the four separate beams is incoherent with respect to the others, and each is aligned so as to overlap on the scaled missile model. One important difference, however, is that—unlike the track illuminator that provides flood illumination of the missile—the adaptive-optics illuminator forms a small spot at a selected location on the missile body, as illustrated earlier in Figure 7. Backscatter from the adaptive-optics illuminator was collected within the same 15-cm aperture used to propagate the scoring beam, and imaged into the wavefront sensor. Output from the wavefront sensor was used to control the surface of a deformable mirror to correct for the instantaneous phasefront error caused by turbulence. When the scoring beam was reflected from this deformable mirror, it was precorrected for the turbulence it experienced as it propagated back to the target.

Minimizing the size of the adaptive-optics illuminator spot on the missile body is an important concern, because the adaptive-optics system performs best when it views light from as small a spot as possible, preferably a diffraction-limited point source. As the size of the adaptive-optics beacon approaches and perhaps exceeds the isoplanatic patch size (the spot size subtended by the isoplanatic angle θ_0), the ability to correct the outgoing scoring beam is reduced. This problem occurs because light originating from different locations within the illuminator spot travels through different atmospheric paths and therefore experiences different turbulence aberrations along the way to the receiver aperture. As a result, the phase measured by the wavefront sensor is not representative of the turbulence-induced phase distortion experienced by the outgoing scoring beam.

Adaptive-Optics Illuminator Comparisons

To quantify the advantages, if any, of using multibeam illumination to provide the adaptive-optics beacon, we made measurements by using either a single adaptive-optics illuminator or a four-beam illuminator. These tests were performed by using active illumination for the adaptive-optics system, while using a point-source beacon for the tracker.

Figure 12 shows the results of these comparisons. The data are scoring-beam Strehl ratio (the ratio of the measured peak intensity to that expected for a diffraction-limited spot) versus Rytov variance for three different configurations. Results obtained by using a single adaptive-optics illuminator are shown as the open triangles; results obtained by using four-beam illumination are shown as solid triangles. For both these cases, tracking was performed by using a point-source beacon. Results obtained by using a point-source beacon for both adaptive optics and tracking are shown by open circles.

Although we collected only a few data points with single-beam illumination, we can draw some tentative conclusions. The two single-beam data points near Rytov variance values of 0.45 and 0.60, respec-

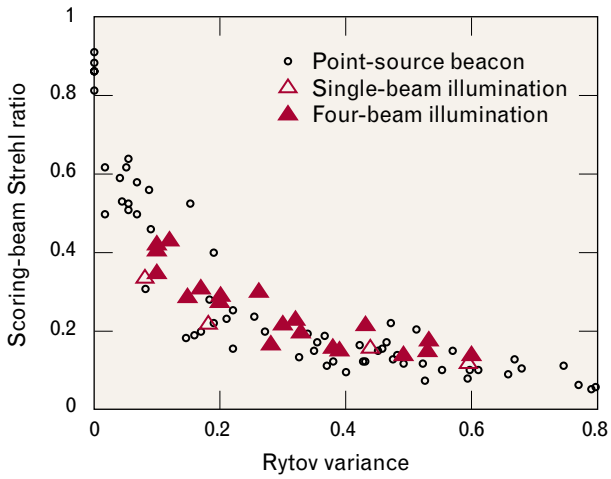

FIGURE 12. Results from adaptive-optics illuminator comparisons. The figure shows the scoring-beam Strehl ratio plotted versus Rytov variance. Results obtained by using a single adaptive-optics illuminator are indicated by the open triangles; results obtained by using four-beam illumination are indicated by solid triangles. The tracker utilized a point-source beacon for both tests. Earlier point-source-beacon results are indicated by the open circles.

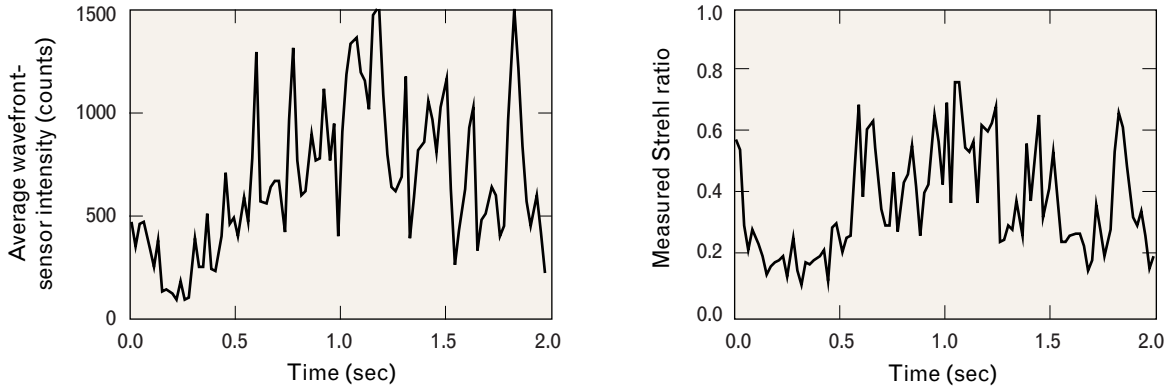

FIGURE 13. Comparison of average wavefront-sensor pupil-plane intensity and scoring-beam Strehl ratio. The left plot shows a two-second temporal history of the average wavefront-sensor pupil-plane irradiance. The data were rebinned to match the 50-Hz recording rate of the scoring-beam diagnostics. The right plot shows scoring-beam Strehl ratio measured during the same two-second period. The degree of temporal correlation between these two signals is most apparent during periods of fading between 0.1 and 0.3 sec.

tively, suggest that single-beam and four-beam performance are approximately the same. The two single-beam data points near Rytov variance values of 0.08 and 0.18, however, suggest a slight decrease in performance when single-beam illumination is used.

We believe this decreased performance results from the signal fading associated with single-beam illumination. Figure 13 shows an example of the performance degradation associated with the fading observed when we use a single-beam adaptive-optics illuminator. The left figure shows a two-second temporal history of the average wavefront-sensor pupil-plane intensity. The wavefront-sensor data were recorded at a frame rate of 2 kHz, but were temporally rebinned to match the 50-Hz recording rate of the scoring-beam far-field irradiance camera. From each frame of the scoring-beam CCD data we computed an instantaneous Strehl ratio. The temporal history of that Strehl ratio is shown in the right side of Figure 13. The degree of temporal correlation between these two signals is most apparent during periods of fading near times from 0.1 to 0.3 seconds.

Illuminator comparisons aside, one striking feature apparent in the results of Figure 12 is the rather low level of performance in general. Strehl ratios over most of the ABL range of interest (Rytov variance approximately 0.1 to 0.5) are between 0.3 and 0.15. We observed this level of performance during our initial point-source beacon tests [2], and attributed the results to strong scintillation that is characteristic of many ABL propagation scenarios. The wavefront-sensor pupil-plane intensity profiles in Figure 14 are examples of this scintillation. The left image shows results obtained with weak turbulence (Rytov variance is approximately 0.05). Although some degree of intensity nonuniformity is evident, the wavefront-sensor pupil is well filled. The right image shows results obtained with stronger turbulence (Rytov variance is approximately 0.4). The intensity scintillation is dramatic; some regions of the wavefront-sensor pupil are saturated, while many other regions are illuminated at levels below what is required to make a good phase measurement. The precise impact of this scintillation on adaptive-optics performance depends on

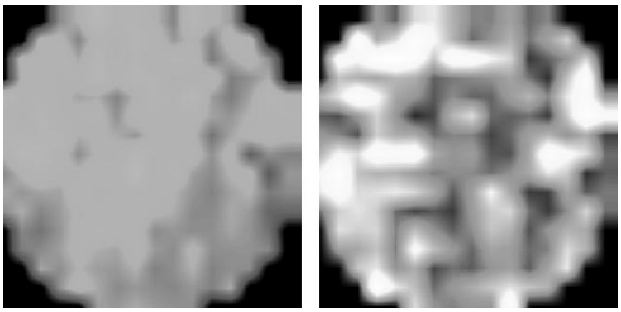

FIGURE 14. Examples of wavefront-sensor pupil-plane intensity profiles. Each image was produced from a single frame of wavefront-sensor subaperture intensity data. The integration time was half a millisecond. The left image was recorded under weak turbulence conditions (Rytov variance approximately 0.05); the right image was recorded during stronger turbulence (Rytov variance approximately 0.4).

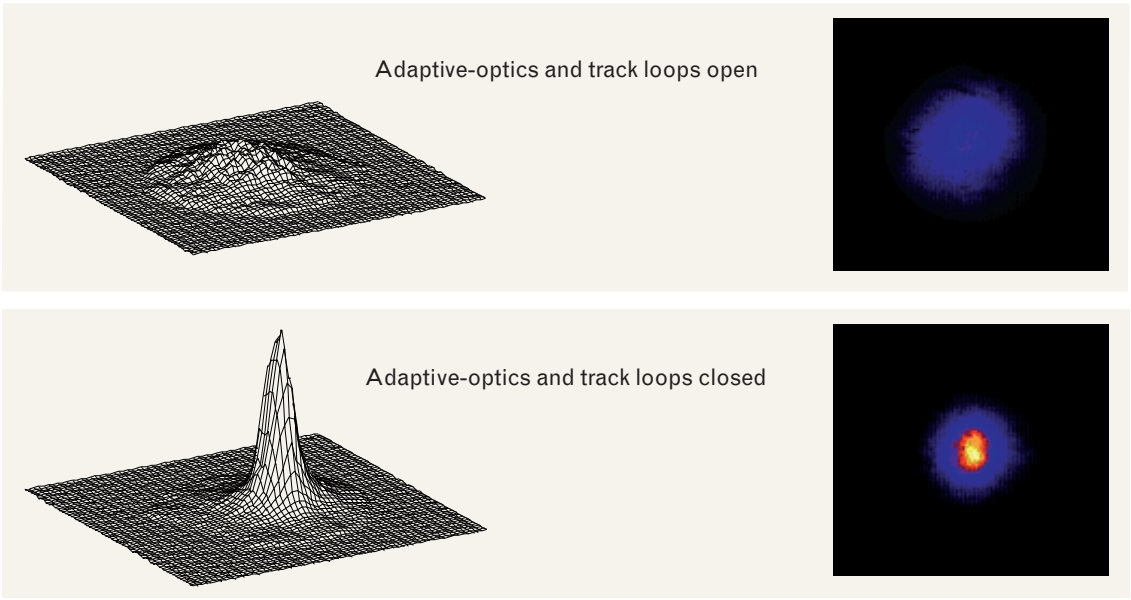

FIGURE 15. Sample results from active compensation with active-tracking tests. The upper plots show a typical scoring-beam far-field irradiance profile obtained without adaptive-optics or tracking correction. The Strehl ratio is approximately 0.04. The lower plots show results obtained when both the adaptive-optics correction and tracking were performed by using active illumination (four-beam illumination for the adaptive optics, and nine-beam illumination for tracking). The Strehl ratio is approximately 0.17. In each case the Rytov variance was approximately 0.6.

such factors as wavefront-sensor dynamic range and noise characteristics, as well as servo temporal bandwidth. Those details are not discussed here. As illustrated in the qualitative examples shown in Figure 14, however, the strong scintillation clearly poses a difficult challenge for the adaptive-optics system.

This source of performance degradation was not unexpected; results from simulations that model the adaptive-optics hardware response to strong scintillation predict similar levels of low performance. In addition, analytical studies [8] show that the scintillation is accompanied by beacon-phasefront discontinuities known as branch points. These studies show that the stronger the scintillation, the higher the probability of branch-point occurrence. Because branch points are not handled properly by conventional adaptive-optics wavefront reconstructors, system performance is degraded by their presence.

Expected ABL Configuration

We conducted a number of tests in which both the adaptive optics and the tracking were performed with active illumination. The adaptive-optics beacon was provided by using four-beam illumination, and tracking was performed by using nine-beam illumination, as shown earlier in Figure 7.

Figure 15 shows sample scoring-beam far-field irradiance profiles. Output from the scoring-beam diagnostics camera was recorded for three seconds and used to form these composite images. The upper half of the figure shows results obtained without either adaptive-optics or tracking compensation. The far-field irradiance profiles are presented as mesh plots (left) and as false-color images (right). The Strehl ratio calculated from the three-second composite image is approximately 0.04. When the adaptive-optics and track loops are closed, we obtain the results shown in the lower half of the figure. In this case, the Strehl ratio calculated from the composite image data has increased to approximately 0.17.

Figure 16, which shows scoring-beam Strehl ratio versus Rytov variance, summarizes the results from many such tests. Results obtained by using active illumination for both adaptive-optics compensation and tracking are shown as solid triangles. For comparison, the figure also shows test results when a point-source beacon was used for both adaptive-optics compensation and tracking (open circles). The point-source-

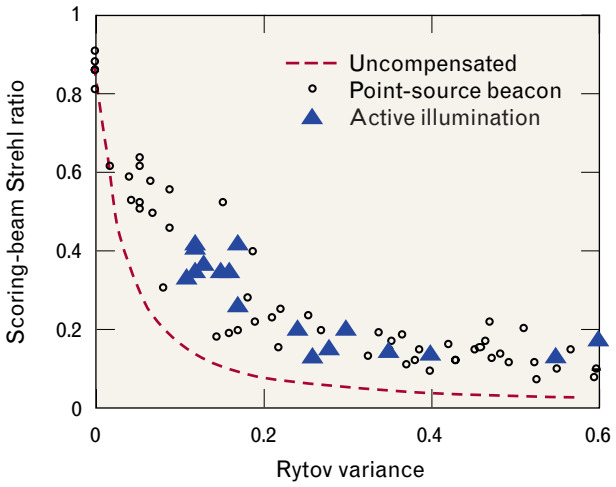

FIGURE 16. Summary of active-compensation results, showing scoring-beam Strehl ratio versus Rytov variance. Results obtained with simultaneous active compensation and active tracking are shown as solid triangles; earlier point-source-beacon results are shown as open circles for comparison. The dashed line indicates the Strehl ratio we would expect without adaptive-optics compensation or tilt correction. These results suggest that the performance of the adaptive-optics system is much the same as the performance achieved by using a point-source beacon.

beacon data values corresponding to a Rytov variance of zero are the results from laboratory bench tests discussed in the appendix. A calculation of the theoretical Strehl ratio without adaptive-optics compensation or tilt correction is shown as a dashed line.

Although there are fewer data points for the active-illumination case, these results suggest that the adaptive-optics system performance is much the same as when a point-source beacon is used.

Summary

We performed propagation experiments across a scaled horizontal laser-propagation path to replicate the turbulence-induced effects anticipated for the ABL. Using this propagation range, we investigated a number of issues related to atmospheric compensation and tracking using active illumination.

We characterized the performance of a multibeam illuminator for tracking, and conducted active-tracking tests using single-beam, four-beam, and nine-beam illumination. Over the range of Rytov variances of interest to the ABL, we observed a nearly two-fold reduction in pointing jitter along the missile's longitudinal axis when nine-beam illumination was used instead of single-beam illumination.

Finally, tests were performed with a configuration closely resembling that planned for the actual ABL system: one multibeam illuminator for tracking and a second multibeam illuminator for adaptive-optics compensation. Results from these experiments demonstrated that conventional adaptive optics and tracking, performed with active illumination of the target missile, are effective in compensating turbulence-induced phase and tilt fluctuations under ABL conditions.

Acknowledgments

This work could not have been completed without the dedicated efforts of other members of the Firepond team. We would like to thank Frank Perry and Paul Szarko for the many hours they spent operating the fire-tower diagnostic system, and Diane Powers for her tireless efforts to align and maintain the adaptive-optics and tracking systems. Robert Hatch helped to maintain the computer networks and data-archival systems. Operation of the Firepond telescope, as well as general site support, was provided by Larry Sweezy and Jan Kansky.

REFERENCES

1. D.P. Greenwood and C.A. Primmerman, "Adaptive Optics Research at Lincoln Laboratory," *Linc. Lab. J.* **5** (1), 1992, pp. 3–24.
2. C.A. Primmerman, T.R. Price, R.A. Humphreys, B.G. Zollars, H.T. Barclay, and J. Herrmann, "Atmospheric-Compensation Experiments in Strong-Scintillation Conditions," *Appl. Opt.* **34** (12), 20 Apr. 1995, pp. 2081–2088.
3. C. Higgs, H. Barclay, S. Cusumano, and K. Billman, "Active Tracking Using Multibeam Illumination," *SPIE* **3381,** 1998, pp. 160–167.
4. C. Higgs, H. Barclay, J. Kansky, D. Murphy, and C.A. Primmerman, "Adaptive-Optics Compensation Using Active Illumination," *SPIE* **3381,** 1998, pp. 47–56.
5. D.L. Fried, "Statistics of Geometric Representation of Wavefront Distortion," *J. Opt. Soc. Am.* **55** (11), 1965, pp. 1427–1435.
6. R.G. Frelich and G.R. Ochs, "Effects of Saturation on the Optical Scintillometer," *Appl. Opt.* **29** (4), 1990, pp. 548–553.
7. C.A. Primmerman, D.V. Murphy, D.A. Page, B.G. Zollars, and H.T. Barclay, "Compensation of Atmospheric Optical Distortion Using a Synthetic Beacon," *Nature* **353,** 12 Sept. 1991, pp. 141–143.
8. D.L. Fried and J.L. Vaughn, "Branch Cuts in the Phase Function," *Appl. Opt.* **31** (11), 1992, pp. 2865–2882.

APPENDIX: BASELINE PERFORMANCE MEASUREMENTS

TO DETERMINE OUR POINTING, tracking, and adaptive-optics performance baseline, we conducted a series of internal calibration tests using a fiber-optic "pseudo-star" point source installed at the *f*/200 focus of the Firepond telescope. This internal-calibration beacon is the diffraction-limited output of a single-mode optical fiber, which can be configured to produce either 488-nm or 514-nm light. Also installed at the *f*/200 focus are a position sensor and a CCD camera similar to those used at the fire tower in Groton, Massachusetts, for target-plane diagnostics. The position sensor and the CCD camera record the tilt and far-field irradiance of the scoring beam when the tracking loops and adaptive-optics loops using the pseudo-star reference source as a beacon are closed. Under benign conditions in the laboratory (no scintillation and little turbulence) the performance measured with these diagnostics represent the best performance we could hope to achieve; these residual errors provide a fundamental measure of our baseline performance. It is important to note, however, that this baseline measurement is relevant only to our current configuration (i.e., servo bandwidth, sensor noise, noncommon path errors, and laboratory sources of mechanical vibration) and does not reflect any fundamental performance limits for the ABL.

In addition to determining performance baselines, we measured the noncommon path tilt errors, i.e., tilt errors experienced by either the scoring beam or the beacon but not both. In our experimental configuration the noncommon path errors arise from two sources: (1) the scoring laser itself, including the optical train that merges the output of the scoring laser into the beacon path, and (2) the tracker optics and the optical train leading to them. Tilt errors arising from both these sources can be measured simultaneously by folding the scoring beam back into the tracker from a point just beyond the tracker's aperture-sharing element.

For each of the tracking algorithms used in the Firepond tests, we measured the noise-equivalent angle [1]. For our typical tracker CCD signal levels, the contribution of the noise-equivalent angle to our baseline performance limit was small but measurable: for example, this angle was in the range of 0.005 to 0.01 λ/D for the windowed centroid algorithm.

Figures 1 and 2 summarize the essential results of our tracker performance tests. In Figure 1 we present typical spectra of the residual jitter when the tracking loops using the pseudo-star point source and the theater missile tracker are closed. In this case the theater missile tracker employed a windowed centroid algorithm at a CCD frame rate of 1961 Hz. Figure 1(a) shows the closed-loop azimuth and elevation spectra calculated from the theater-missile-tracker data. The residual rms jitters are small: 0.027 λ/D for azimuth and 0.083 λ/D for elevation (because of the field-of-view rotation caused by the Coudé path, the elevation axis corresponds to the missile's transverse axis). The most notable features in these spectra are the tilts at frequencies near 30 and 60 Hz. Both the azimuth and elevation spectra contain a significant amount of power, with the elevation spectra containing the most power. We identified the origin of this tilt as arising from a mechanical vibration. The primary contribution to this vibration comes from a platform supporting a portion of the telescope that merges the 12-cm deformable-mirror beampath into the *f*/200 cone of the Firepond telescope. Because the 0-dB crossover in the theater-missile-tracker error-rejection computation is at approximately 90 Hz, little error rejection of this source of tilt error is possible.

Figure 1(b) shows the corresponding scoring-beam tilt spectra calculated from data recorded by the *f*/200 diagnostics on the laboratory bench. In this case the residual errors are somewhat larger than the residuals reported by the theater missile tracker. The scoring-beam azimuth and elevation rms jitters are 0.076 and 0.098 λ/D, respectively. In addition to the larger residual errors, the shape of the tilt spectra are

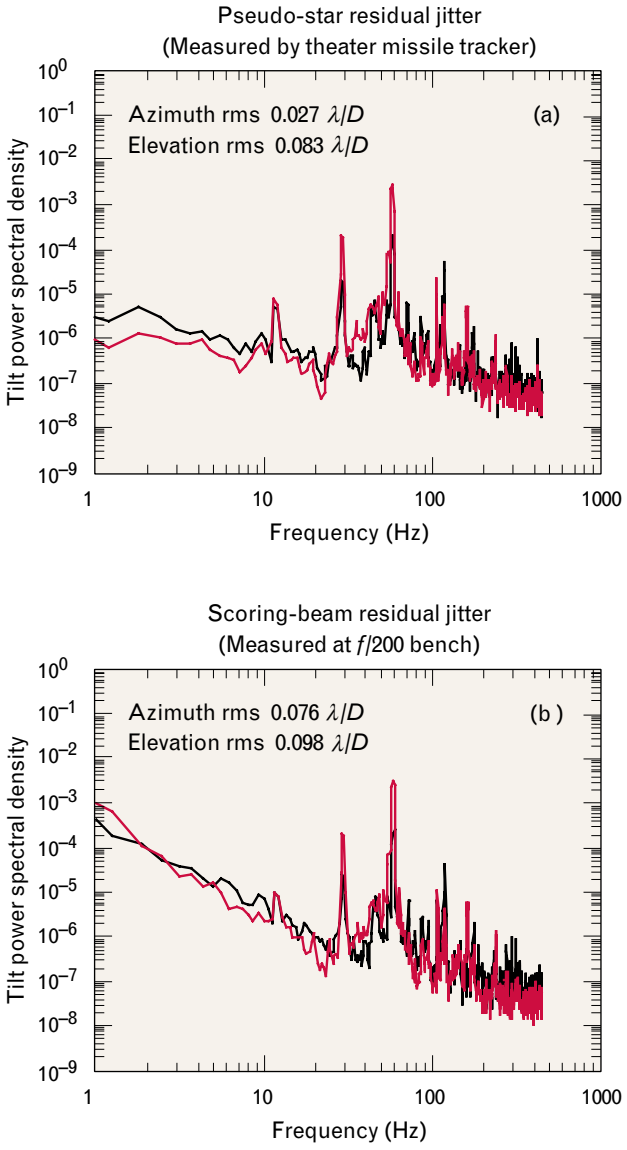

FIGURE 1. Residual tilt spectra from internal calibration tests: (a) the spectrum of the residual tilt on the internal pseudo-star point source as measured by the theater missile tracker; (b) the residual tilt spectra remaining on the scoring beam as measured by the *f*/200 diagnostics on the laboratory bench. In both cases, spectra for the elevation axis are drawn as a red line and spectra for the azimuth axis are drawn as a black line. The rms tilt jitters for azimuth and elevation are also indicated.

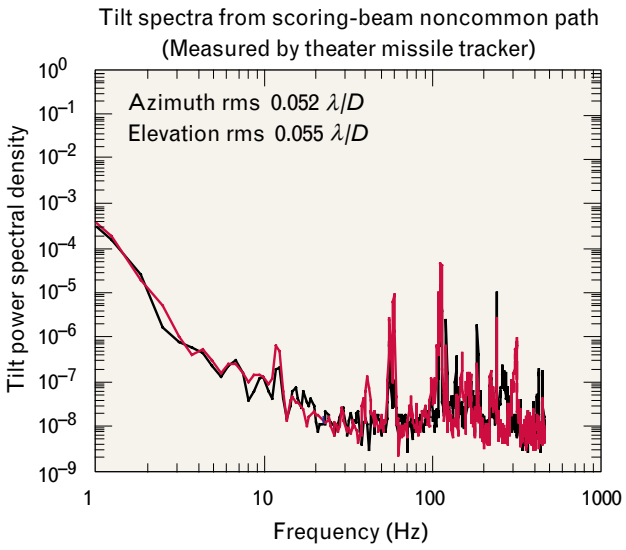

FIGURE 2. Tilt spectra for scoring-beam noncommon path. Tilt-jitter data were recorded for the scoring-beam noncommon path (the path not sampled by the return beacon), and tilt spectra were calculated. The elevation axis is shown by the red line. The rms jitter values for azimuth and elevation are also indicated.

different. In particular, the spectra contain more power at frequencies below 10 Hz. This increase in power at low frequency comes from the scoring-beam noncommon path errors, as shown in Figure 2. Although the scoring-beam noncommon path jitter is low (approximately 0.053 λ/D per axis) nearly all of it is at low frequency.

By combining the measured rms scoring-beam noncommon path jitter and the rms residual jitter on the pseudo-star point source, we can estimate the expected closed-loop performance of our baseline system. For the data just described, the root-sum-square addition of these two errors yields approximately 0.06 λ/D for azimuth and 0.10 λ/D for elevation. These estimates are in reasonable agreement with the measured scoring-beam residual rms pointing jitters.

We performed baseline performance measurements many times during this test period. The overall average of the results from such tests provides a good estimate of our scoring-beam pointing jitter performance limits. These limits are 0.075 λ/D for the axis corresponding to the missile's longitudinal axis, and 0.12 λ/D for the missile's transverse axis.

The same fiber-optic "pseudo-star" was utilized to measure the performance baseline for the adaptive-optics system. Figure 3 shows sample results from those tests. The left figure shows a typical scoring-beam focal-plane irradiance profile obtained with the pseudo-star beacon when the adaptive-optics and

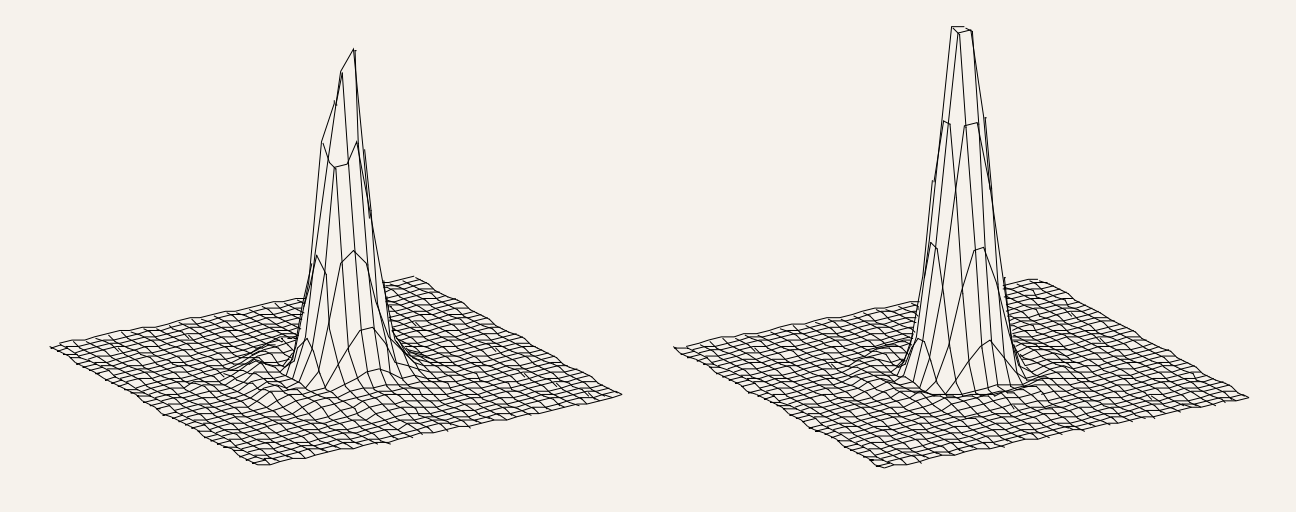

FIGURE 3. The figure on the left shows the measured scoring-beam profile (Strehl = 0.90) recorded on the adaptive-optics laboratory bench for the pseudo-star point-source beacon, without the effects of atmospheric turbulence and scintillation. The figure on the right shows the calculated ideal diffracted-limited irradiance profile (Strehl = 1.0).

track loops are closed. This irradiance profile was determined from a 128-frame sequence recorded over a three-second interval. The measured Strehl ratio of 0.90 provides a measurement of adaptive-optics and tracking-system performance in the absence of atmospheric turbulence. Other laboratory measurements indicate this slightly degraded baseline performance is the result of a noncommon path error in the diagnostic optics and a residual uncorrectable error on the surface of the deformable mirror. For comparison, the image on the right in Figure 3 shows the calculated ideal diffraction-limited focal-plane irradiance (Strehl ratio = 1.0) we would observe for the same total flux.

REFERENCES

1. S. Cusumano and C. Higgs, "The Noise Equivalent Angle of the Windowed Algorithms," LIAE Internal Report, Air Force Phillips Laboratory, 21 Aug. 1996.

CHARLES HIGGS
is a staff member in the Laser and Sensor Applications group. His research interests are in the areas of adaptive and nonlinear optics. Currently, he is heading an effort to construct an airborne payload for airborne-laser tests against a dynamic target. He received a B.S. degree in physics from Miami University (Ohio) and a Ph.D. in physics from Rice University.

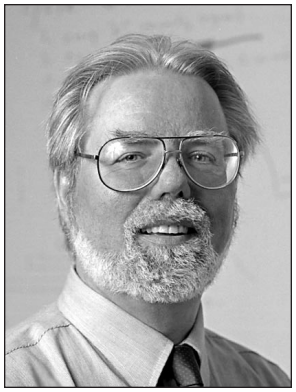

HERBERT T. BARCLAY
is an associate staff member in the Laser and Sensor Applications group. His area of research is atmospheric-turbulence correction with adaptive optics. He received a B.A. degree in physics and an M.S.E.E. degree in electro-optics from Northeastern University. Before joining Lincoln Laboratory in 1985 he worked at the Frances Bitter National Magnet Laboratory at MIT.

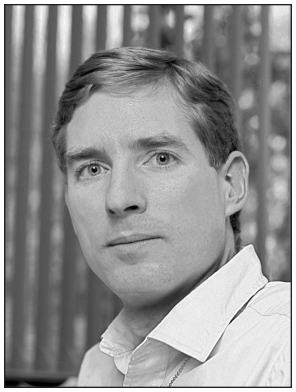

DANIEL V. MURPHY
is an assistant leader of the Laser and Sensor Applications group. He received a B.A. degree in physics from Amherst College and a Ph.D. degree in engineering and applied science from Yale University.

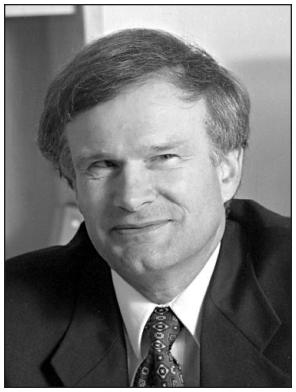

CHARLES A. PRIMMERMAN
is leader of the Laser and Sensor Applications group. He received an A.B. degree in physics from Duke University and S.M. and Ph.D. degrees in nuclear engineering from MIT.